



HAL
open science

Magnetism of Iron Oxide Nanoparticles: From Atomic Order to Complexity at the Mesoscopic Scale

Marie Darcheville, Anne-lise Adenot-engelvin, Christophe Boscher, Jean-Marc Greneche, Christophe Lefèvre, Jérôme Robert, Ovidiu Ersen, José M González-Calbet, Maria Luisa Ruiz Gonzalez, André Thiaville, et al.

► **To cite this version:**

Marie Darcheville, Anne-lise Adenot-engelvin, Christophe Boscher, Jean-Marc Greneche, Christophe Lefèvre, et al.. Magnetism of Iron Oxide Nanoparticles: From Atomic Order to Complexity at the Mesoscopic Scale. *physica status solidi (RRL) - Rapid Research Letters*, In press, 10.1002/pssr.202400059 . hal-04760744

HAL Id: hal-04760744

<https://hal.science/hal-04760744v1>

Submitted on 30 Oct 2024

HAL is a multi-disciplinary open access archive for the deposit and dissemination of scientific research documents, whether they are published or not. The documents may come from teaching and research institutions in France or abroad, or from public or private research centers.

L'archive ouverte pluridisciplinaire **HAL**, est destinée au dépôt et à la diffusion de documents scientifiques de niveau recherche, publiés ou non, émanant des établissements d'enseignement et de recherche français ou étrangers, des laboratoires publics ou privés.

Magnetism of Iron Oxide Nanoparticles: From Atomic Order to Complexity at the Mesoscopic Scale

Marie Darcheville, Anne-Lise Adenot-Engelvin,* Christophe Boscher, Jean-Marc Grenèche, Christophe Lefèvre, Jérôme Robert, Ovidiu Ersen, José Maria Gonzalez Calbet, Maria Luisa Ruiz Gonzalez, André Thiaville, and Clément Sanchez

Zn-substituted iron oxide nanoparticles of ≈ 5 nm in diameter are synthesized by a microwave-assisted thermal decomposition method. The addition of ethylene glycol results in a size increase to 22 nm. Cationic disorder has been observed by electron energy loss spectroscopy–scanning transmission electron microscopy. Using Mössbauer spectrometry combined with Rietveld analysis, the complete cationic and vacancies repartition in the lattice is determined, as well as the canting of magnetic moments. This allows the magnetic moment to be calculated, in good agreement with that measured. The alternating current magnetic susceptibility is modeled by the Néel–Brown and the Coffey models, showing some discrepancy between these two approaches which is discussed. The largest particles show a complex morphology involving an oriented attachment mechanism of smaller units. Their cationic disorder and internal porosity have been evidenced and quantified, and the work shows that despite these defects they behave rather as magnetically blocked nanoparticles.

strongly influence the spin texture.^[4] Here we study nanoparticles synthesized by a microwave-assisted thermal decomposition (MATD)^[5] method, which is easier and faster than classical thermal decomposition, while providing similar characteristics (size dispersion, yield, etc.).

The iron oxide composition was chosen as $\text{Zn}_{0.4}\text{Fe}_{2.6}\text{O}_4$ in order to maximize magnetization: for bulk materials, Zn-substitution up to ≈ 0.5 atomic fraction of Zn in Fe_3O_4 increases the net ferrimagnetic magnetization expressed as the difference between octahedral (B)-sublattice magnetization and tetrahedral (A)-sublattice magnetization, since the repartition of cations on both sites is written $(\text{Zn}_{0.4}^{2+}\text{Fe}_{0.6}^{3+})[\text{Fe}_{0.6}^{2+}\text{Fe}_{1.4}^{3+}]\text{O}_4$ by using the usual notation with round brackets () for the tetrahedral A sites and square brackets [] for the B sites. Indeed, the preferred location


of Zn^{2+} in the A sublattice decreases its magnetization while the resulting increase in Fe^{3+} cations in the B sublattice increases its magnetization.^[6] It has, however, long been known that the cationic distribution in nonequilibrium samples such as fast-cooled bulk ferrites^[7] deviates from the theoretical one and can be tuned by the elaboration process in thin films^[8] or in nanoparticles.^[9,10] Moreover, in the latter case, oxidation of Fe^{2+} into Fe^{3+} occurs^[10] and has to be taken into account to

1. Introduction and Propose

Iron oxide nanoparticles are widely studied for biomedical applications^[1] such as magnetic hyperthermia^[2] or magnetic resonance imaging, or as starting powders used in advanced processes such as additive manufacturing.^[3] Their magnetic properties depend not only on the oxide composition but also on their geometrical characteristics (morphology and size), which can

M. Darcheville, A.-L. Adenot-Engelvin, C. Boscher
CEA-DAM Le Ripault
BP 16, 37260 Monts, France
E-mail: anne-lise.adenot-engelvin@cea.fr

J.-M. Grenèche
Faculté des Sciences & Techniques Avenue Olivier Messiaen
Institut Matériaux et Molécules du Mans
UMR CNRS 6283, Avenue Olivier Messiaen, 72085 Le Mans Cedex 09, France

 The ORCID identification number(s) for the author(s) of this article can be found under <https://doi.org/10.1002/pssr.202400059>.

© 2024 The Author(s). physica status solidi (RRL) Rapid Research Letters published by Wiley-VCH GmbH. This is an open access article under the terms of the Creative Commons Attribution-NonCommercial License, which permits use, distribution and reproduction in any medium, provided the original work is properly cited and is not used for commercial purposes.

DOI: 10.1002/pssr.202400059

C. Lefèvre, J. Robert, O. Ersen
Institut de Physique et Chimie des Matériaux de Strasbourg
Université de Strasbourg, CNRS
23 rue du Loess (Bât. 69) BP 43, 67034 Strasbourg Cedex 2, France

J. M. Gonzalez Calbet, M. L. Ruiz Gonzalez
Departamento Química Inorgánica
Facultad de Químicas
Universidad Complutense
28040 Madrid, Spain

A. Thiaville
Laboratoire de Physique des Solides
Université Paris-Saclay
CNRS UMR 8502, 91400 Orsay, France

C. Sanchez
Laboratoire Chimie de la Matière Condensée de Paris
UPMC-CNRS-Collège de France
75252 Paris Cedex 05, France

determine the actual composition of the substituted iron oxide. In this study, several chemical and structural characterizations, and in particular ^{57}Fe Mössbauer spectrometry, have been performed to clarify the atomic order of the spinel constituting these nanoparticles in order to compare to the measured magnetic moment.

Adjusting the size of the nanoparticles in thermal decomposition methods can be achieved by tuning the boiling point of the solvent^[11] or the ligand to solvent ratio. In MATD, the solvent is less easy to change due to requirements on dielectric constant and vapor pressure.^[12] Here, we chose to increase the nanoparticle size up to ≈ 25 nm (higher than the expected superparamagnetic critical size) by adding ethylene-glycol (EG). This way has been reported in water or organic media, with polyol^[13] and solvothermal^[14,15] synthesis. Whatever the route or the precursor (salt or organo-metallic), it results in complex, hollow, and mesostructured nanoparticles, called “spherulite” or “raspberry-like”, in which spherical nanocrystals stick together to form a hollow meso-bowl of ≈ 100 nm diameter. This phenomenon has been attributed to an EG-driven polyol reaction occurring after precipitation of the nanocrystals.^[13] When applied to MATD,^[16] the hollow internal structure has not been evidenced, possibly because the size of the particles (≈ 20 nm) was too small compared to the scanning electron microscope (SEM) resolution. Here, transmission electron microscope (TEM) tomography^[17] has been used to assess the inner morphology of nanoparticles. In addition, field-cooled (FC) and zero-field cooled (ZFC) magnetization curves and alternating current (AC) magnetic susceptibility have been measured to observe the effect of the mesostructure on the magnetic ordering of the nanoparticles. An overview of the work is sketched in **Figure 1**.

The paper is organized as follows: the results on small nanoparticles (referred to as SP) synthesized, as described in the Experimental Section, without EG addition are first presented and interpreted, as a simple case. Then, the characteristics observed on larger nanoparticles (referred to as LP) synthesized with EG addition are discussed within the framework introduced for SP and compared to literature results on dense or hollow nanoparticles.

2. Results and Discussion

2.1. SP Nanoparticles

The Zn/Fe ratio of the ferrite was determined by global chemical characterization using inductively coupled plasma–atomic emission spectroscopy, and at different scales by energy-dispersive spectroscopy (EDS)-SEM and EDS-TEM. It was found to be $\text{Zn}_{0.38}\text{Fe}_{2.62}\text{O}_4$, in agreement with the theoretical ratio given by the relative proportion of the acetyl-acetonate reactants, within experimental error, whereas in classical thermal decomposition, deviations from stoichiometry are encountered.^[18] X-ray diffraction (XRD) was performed, showing only the spinel phase with a lattice parameter of 0.8396(2) nm. Our observed value is consistent with existing literature comparing nanoparticles and their bulk counterparts.^[19] It is important to note that the cell parameter is not only affected by the chosen synthesis method but also by the specific cation distribution within the material.^[20] Rietveld analysis gave a mean crystallite diameter of 4 ± 1 nm. TEM image analysis gave a mean particle diameter of 6.1 nm with a standard deviation of 1.0 nm, in agreement with the XRD diameter, as shown in **Figure 2**.

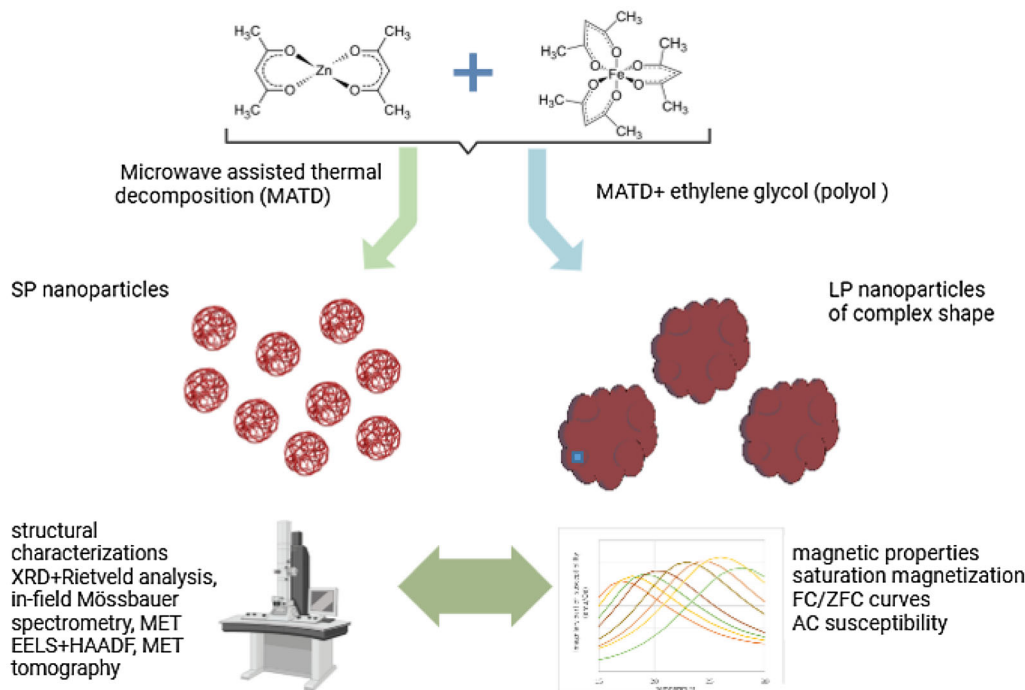


Figure 1. Graphical overview of the work.

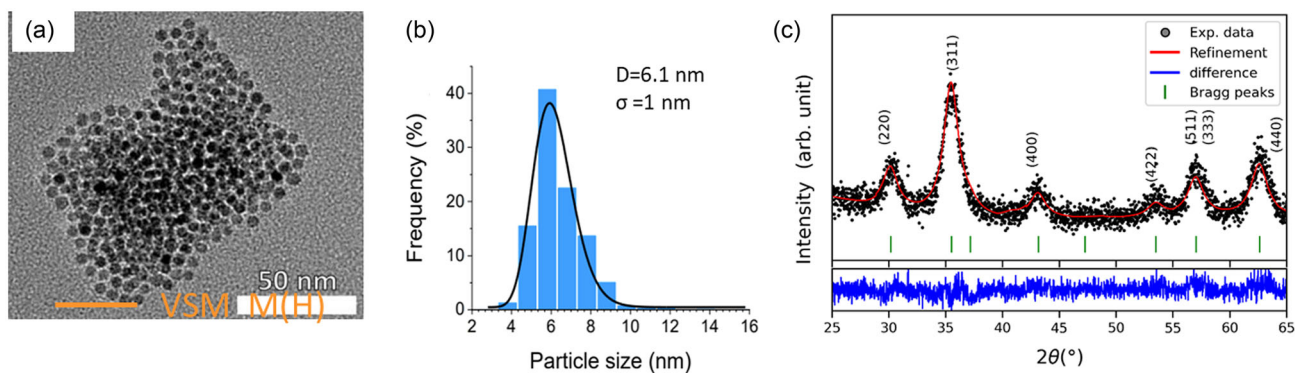


Figure 2. a) Transmission electron micrograph, b) size distribution allowing to determine a mean size of 6.1 nm with a standard error of 1 nm, and c) X-ray diffractogram with its Rietveld description, for the SP sample.

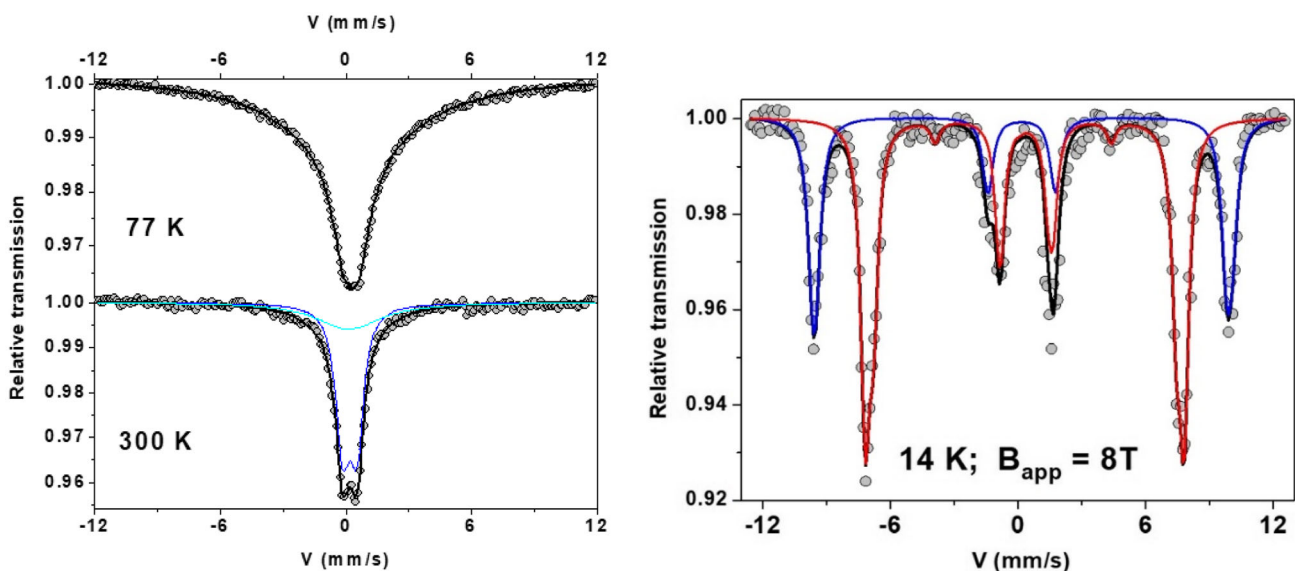


Figure 3. Mössbauer spectra of SP nanoparticles in zero-field at 77 and 300 K (left) and under applied field of 8 T (right) at 14 K: blue and red lines stand for the Fe^{3+} species located, respectively, in tetrahedral and octahedral sites.

Mössbauer spectra of the SP sample recorded in various conditions are shown in **Figure 3**. The fitting model at 300 K consists in a quadrupolar doublet and a broad single line to describe the symmetrical wings, while that of the 77 K spectrum results in a very wide single line component. The symmetry of the hyperfine structures at 300 and 77 K is consistent with a unique oxidation state, i.e., Fe^{3+} , according to the value of the isomer shift δ_{Fe} (0.32 mm s^{-1} at 300 K). To retrieve the distribution of Fe^{3+} in the A and B sites, and estimate the canting angle of these respective magnetic moments, in-field Mössbauer experiments were performed. Indeed, one can follow the action of the external magnetic field from the intensities of the intermediate lines of the sextet and the evolution of the magnetic splitting which corresponds to the effective magnetic field B_{eff} at the ^{57}Fe nucleus. This field is the vectorial sum of the hyperfine field B_{hf} and the external magnetic field B_{app} , as explained in Section 4. In the case of a ferrimagnetic order, one expects a splitting into two magnetic components describing the parallel and antiparallel

magnetic Fe moments with respect to the external magnetic field, provided a sufficiently large external field of at least 6–7 T is applied. It is also important to mention that a significant contribution from the negative Fermi contact term is expected in Fe^{3+} oxides ($S = 5/2$), leading to a hyperfine field rather antiparallel to the magnetic moment, which is confirmed by in-field Mössbauer experiments. Consequently, analysis of the in-field spectrum provides the values of B_{eff} at the different Fe sites, their respective canting angle θ between the Fe magnetic moments and the applied field, and their isomer shift δ_{Fe} and quadrupole shift $2e$. The values of the hyperfine field can be estimated using the following equation

$$B_{\text{hf}}^2 = B_{\text{eff}}^2 + B_{\text{app}}^2 - 2B_{\text{eff}}B_{\text{app}}\cos\theta \quad (1)$$

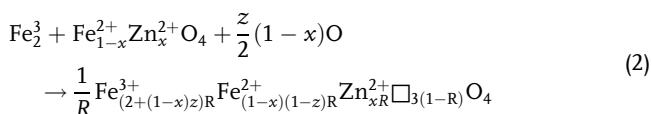
The absorption area of the peaks expresses the proportion of each iron species (see **Table 1** in Section 4).

Table 1. Parameters used for SP and LP nanoparticles to fit the Mössbauer spectra.

Sample	Fe site	δ_{Fe} [mm s ⁻¹]	2ϵ [mm s ⁻¹]	B_{eff} [T]	Θ [°]	B_{hf} [T]	Absorption
		±0.05	±0.05	±0.5	±5	±0.5	Area (±1)
SP	Fe ³⁺ A	0.37	0.00	60.3	2	52.3	35.6
	Fe ³⁺ B	0.53	0.00	45.5	15	53.3	64.4
0.2LP	Fe ³⁺ A	0.37	0.00	60.1	0	52.1	30.7
	Fe ³⁺ B	0.55	0.00	45.2	15	53.0	46.2
	Fe ²⁺	1.15	-0.64	39.4	29	32.7	23.1
0.4LP	Fe ³⁺ A	0.38	0.00	59.8	0	51.8	29.4
	Fe ³⁺ B	0.55	0.00	44.8	17	52.5	58.9
	Fe ²⁺	1.15	-0.20	37.9	16	30.3	11.7

Table 2 presents the main characteristics determined on SP sample: to retrieve the actual cationic distribution on A and B sites, we combined Mössbauer results for the iron species with Rietveld analysis for Zn and vacancies.

The partial oxidation of the substituted magnetite is described through the O'Reilly formalism^[21,22] with the following equation:



In this formula, $x = 0.4$ is the Zn²⁺ atomic fraction, z is the oxidation degree $z = 1 - x_{\text{Fe}^{2+}}$, where $x_{\text{Fe}^{2+}}$ is the Mössbauer

absorption area of Fe²⁺ and $R = \frac{8}{8+z(1-x)}$. Labeling the total amount of Fe in the formal spinel structure by $t_{\text{Fe}} = R(3-x)$, the atomic fractions are $x_{\text{Fe}_A^{3+}} = \frac{n_{\text{Fe}_A^{3+}}}{t_{\text{Fe}}}$ and $x_{\text{Fe}_B^{3+}} = \frac{n_{\text{Fe}_B^{3+}}}{t_{\text{Fe}}}$ where $n_{\text{Fe}_A^{3+}}$ is the molar fraction of Fe³⁺ in A site in the equivalent spinel, leading to the actual composition (Fe_{0.86}³⁺)[Fe₀²⁺Fe_{1.56}³⁺]Zn_{0.38}□_{0.21}O₄. All the Fe²⁺ were converted into Fe³⁺ (full oxidation) as a result of the diffusion of O inside the whole volume of this small size nanoparticle. Starting from this formula, the final Rietveld analysis of the SP compound was performed: the free parameters were thus the lattice parameter of 0.8396(2) nm, the zinc distribution between octahedral and tetrahedral sites, and the crystallite size. The results of the refinements lead to the following chemical formulation (Fe_{0.86}³⁺Zn_{0.09}□_{0.05})[Fe₀²⁺Fe_{1.56}³⁺Zn_{0.28}□_{0.16}]O₄ giving the quantitative distribution of Zn²⁺ and vacancies on A and B sites. The X-ray density was then computed from the actual molar mass deduced from the chemical formula and the lattice volume from the lattice parameter and was used to convert specific magnetization (after correction from for the weight fraction of OA coating given in Section 4) into magnetic moment density.

We now discuss the magnetic properties. **Figure 4** shows the measured vibrating sample magnetometer (VSM) loop at room temperature and the FC/ZFC magnetization curves. First, we focus on the magnetic moment for which the measured value is 3.41 μ_B per formula unit (f.u.) (see Table 2). This value depends on both the magnetic moment of the ferrimagnetic sublattices and on the disorientation expressed by the canting angle. In magnetic nanoparticles, the canting angle determined from in-field Mössbauer spectrometry is often converted into a surface layer thickness assuming a strong magnetic disorder only at the

Table 2. Size, cationic distribution, and magnetic moment for SP nanoparticles.

Size [nm]	Cationic distribution	Magnetic Moment (at 2 K) μ _B /f.u.
from TEM 6.1 ± 1	Theoretical (Zn _{0.4} Fe _{0.6} ³⁺)[Fe _{0.6} Fe _{1.4} ³⁺]O ₄	Measured 3.41
From Rietveld 4 ± 1	From Mössbauer (Fe _{0.86} ³⁺)[Fe ₀ ²⁺ Fe _{1.56} ³⁺]Zn _{0.38} □ _{0.21} O ₄	Computed 3.22
From Langevin ≈ 5	Completed with Rietveld (Fe _{0.86} ³⁺ Zn _{0.09} □ _{0.05})[Fe ₀ ²⁺ Fe _{1.56} ³⁺ Zn _{0.28} □ _{0.16}]O ₄	-

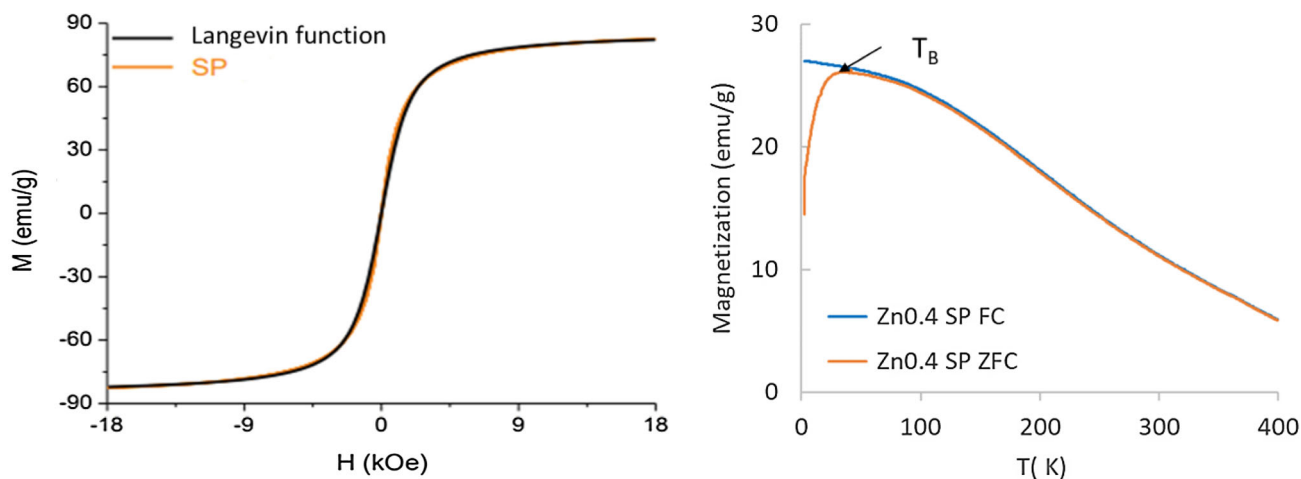


Figure 4. Left, room temperature VSM loop fitted with a Langevin function using $M_s = 85.6 \text{ emu g}^{-1}$ and $d = 5 \text{ nm}$ and, right, ZFC/FC curves of SP sample.

surface. In this way, the thickness e of the disordered layer can be estimated through the following relation: $e = (r/2) \times \sin^2(\theta)$ with r the mean radius of the nanoparticles.^[23] From the measured Fe_B^{3+} canting angle of 15° , with $r = 3.2$ nm, one obtains $e = 0.1$ nm. This thickness is very small and seems unphysical in comparison with values found for other iron oxide nanoparticles^[11] which are around a unit lattice cell of either magnetite or maghemite (0.8 nm). Moreover, it has been recently proposed that the organic surfactant at the surface of the nanoparticles can reduce the surface cationic hence magnetic disorder.^[24]

Here, as described by the Yafet–Kittel model,^[25,26] the high content of nonmagnetic species (vacancies (0.21) and nonmagnetic Zn^{2+} cations (0.38)) may lead to a local strong spin disorder expressed as a mean volume canting, as evidenced for maghemite nanoparticles larger than 5 nm.^[27] A more accurate description would involve a localized canting for cations neighboring a nonmagnetic species^[28] rather the mean canting angle used in the Yafet–Kittel.

The magnetic moment $M_{\text{SP the0}}$ is then computed from the atomic fraction of each magnetic species, and the mean canting angle determined by Mössbauer spectrometry and the spin S and g values of each magnetic cation: Fe^{3+} (2.5 and 2 resp.) and Fe^{2+} (2 and 2.1 resp.):

$$M_{\text{SP the0}} = M_B - M_A = n_{\text{Fe}_B^{3+}} \cdot \cos \theta_{\text{Fe}_B^{3+}} \cdot g_{\text{Fe}_B^{3+}} \cdot S_{\text{Fe}_B^{3+}} + n_{\text{Fe}_B^{2+}} \cdot \cos \theta_{\text{Fe}_B^{2+}} \cdot g_{\text{Fe}_B^{2+}} \cdot S_{\text{Fe}_B^{2+}} - n_{\text{Fe}_A^{3+}} \cdot g_{\text{Fe}_A^{3+}} \cdot S_{\text{Fe}_A^{3+}} \quad (3)$$

Comparing with the measured magnetic moment $M_{\text{SP exp}}$ deduced from the saturation magnetization, the agreement is fairly good (5.6% discrepancy).

Going to the nanoparticle scale, the VSM hysteresis loop at 300 K is typical of a superparamagnetic state and was fitted by a Langevin function with a particle diameter of 5 nm in accordance with Rietveld size determination (Figure 4). The Mössbauer spectra at 77 and 300 K (Figure 3) exhibit mainly a single broad peak consistent with the superparamagnetic state. The small size, a distribution of size, and dipolar interactions between the nanoparticles may be responsible for the weak doublet observed at 300 K instead of a single peak.^[29]

Through FC/ZFC magnetization measurements, a characteristic temperature T_B of about 30 K, can be determined as the temperature at which ZFC and FC curves start to diverge and will be referred to as the “blocking temperature” in the following. As established by^[30], a better way to determine the blocking temperature requires to compute the derivative of $(M_{\text{ZFC}} - M_{\text{FC}})$ to obtain the blocking temperature distribution, but here the AC susceptibility signal was too noisy to be used for this purpose. In addition, the AC susceptibility was measured in the 15–50 K temperature range. The Néel–Brown relation $\tau = \tau_0 \exp \frac{E_b}{k_B T}$ where E_b is the barrier energy of the superparamagnetic relaxation, also expressed as $K_{\text{eff}} V$ where V is the volume of the nanoparticle (taking for SP diameter the mean value of 5 nm), was applied to describe the temperature of the maximum imaginary susceptibility $T_{\chi''_{\text{max}}}$ versus the measurement time $\tau = \frac{1}{2\pi f}$ (Figure 9c). From this model, as shown in Figure 9c, values for K_{eff} of $\approx 100 \text{ kJ m}^{-3}$ at a temperature of ≈ 30 K and τ_0 of 1.08×10^{-8} s were determined. From these values, and using

the measuring time of 2 s for acquisition of the ZC/ZFC curves, the computed value of $T_B = \frac{K_{\text{eff}} V}{k_B \ln(\frac{V}{\tau_0})}$, 25 K, is determined, in agreement with that inferred from FC/ZFC measurements.

In another study of Fe_3O_4 nanoparticles of 5 nm diameter, close to our SP,^[31] a much higher value of K_{eff} of $\approx 350 \text{ kJ m}^{-3}$ was found, which was attributed to interparticle interactions together with a very low τ_0 of 10^{-13} s. In our case, τ_0 is larger by several orders of magnitude so that dipolar interactions should not be important.

To confirm this assumption, the following expression $E_d = \frac{\mu_0}{4\pi} n_1 \frac{\mu^2}{d^3}$ was used to compute the dipolar coupling energy^[32] contribution to the barrier energy, where n_1 is the number of first-neighboring particles (usually 12 in a close-packed arrangement), $\mu = M_s V$ is the magnetic moment of the nanoparticle with $M_s = 445 \text{ kA m}^{-1}$, and d is the interparticle distance. This last one is estimated at 10 nm (the sum of the external diameter of the nanoparticle: 6.1 nm and 2 times the thickness of the oleate coating of 2 nm). Then, the dipolar coupling energy could be estimated to be ≈ 70 K, which can be neglected since $E_b/k_B = 482$ K. The difference (87 kJ m^{-3}) between the contribution of the dipolar coupling of 13 kJ m^{-3} and the energy barrier E_b (100 kJ m^{-3}) can be interpreted as an effective anisotropy energy. Most of the energy barrier seems to be then mainly due to the magnetocrystalline anisotropy energy (MAE).

MAE of bulk iron oxides^[33] is for magnetite 13.5 kJ m^{-3} and for substituted magnetite^[34] $\text{Zn}_{0.4}\text{Fe}_{2.6}\text{O}_4$ 3 kJ m^{-3} at room temperature, increasing to $15\text{--}20 \text{ kJ m}^{-3}$ at 90 K in the last case, since anisotropy increases when temperature decreases. For $\gamma\text{-Fe}_2\text{O}_3$, which is close to our composition since it is fully oxidized, we have 47 kJ m^{-3} ^[33] at room temperature. Substitution by Zn^{2+} in maghemite should decrease the value of MAE by “dilution” with nonmagnetic Zn^{2+} in accordance with molecular field theory: if it follows the same variation as for magnetite,^[34] it could be 4 times smaller, so close to $\approx 10 \text{ kJ m}^{-3}$ at room temperature. As the anisotropy we determined is at ≈ 30 K, the effect of temperature on the MAE, which is of 5 times higher at 90 K for $\text{Zn}_{0.4}\text{Fe}_{2.6}\text{O}_4$, could then increase it up to $\approx 50 \text{ kJ m}^{-3}$. In conclusion, the main contribution to the effective anisotropy energy seems to be the MAE, taking into account both the decrease due to nonmagnetic substitution and enhancement due to temperature.

The SP τ_0 of 1.08×10^{-8} s does not match with the usual range of values [10^{-9} to 10^{-11} s] generally given by authors. Deviations of τ_0 are commonly found with times shorter than 10^{-11} s and attributed to dipolar interactions^[31] or to spin glass-like magnetic states.^[35] Here, dipolar interactions can be a priori neglected as discussed previously. Following Coffey,^[36] we computed the characteristic time $\tau_N = \frac{1+\alpha^2}{2\alpha} \frac{M_s V}{\gamma k_B T}$, where γ is the gyromagnetic ratio ($1.76 \times 10^{11} \text{ Hz T}^{-1}$), $T \approx 30$ K and α is the damping constant from the Landau–Lifshitz–Gilbert equation. Taking $\alpha = 0.05$, slightly larger than the measured value for perfect magnetite films,^[37,38] we find $\tau_N = 3.86 \cdot 10^{-9}$ s. Then by solving $\frac{\tau_0}{\tau_N} = \frac{\sqrt{\pi}}{2} \sigma^{-3/2} e^{\sigma}$ (where the parallel relaxation time $\tau_0 = 1.08 \cdot 10^{-8}$ s is the SP measured one), we determine $\sigma \cong 2.6$ and with $\sigma = \frac{K_{\text{eff}} V}{k_B T}$ a value of $\approx 16 \text{ kJ m}^{-3}$ for K_{eff} , 5 times smaller than the $\approx 100 \text{ kJ m}^{-3}$ determined with the energy barrier.

The discrepancy between the energy barrier determined from the Néel–Brown model and the Coffey model, which involves the Landau–Lifshitz–Gilbert equation and takes into account the magnetization dynamics, may lie in the assumptions of this model: uniaxial anisotropy, noninteracting particles. The coupling between particles cannot be handled by computing the static dipolar energy. In the measured samples consisting of SP nanoparticles coupled by a weak static dipolar energy, dynamic stray fields during the relaxation of one particle could influence the effective field experienced by the neighboring nanoparticles, which can be then smaller than from the effective field assumed in Coffey’s model. Experimentally, it is difficult to synthesize samples of noninteracting nanoparticles: even if the volume fraction is low, nanoparticles form clusters with strong local interactions.

To summarize this part, the magnetic properties of SP have been successfully described from the atomic to the nanoparticle scale thanks to extensive structural and magnetic characterizations. The magnetic moment has been understood from the actual chemical order in the spinel, assuming a moment reduction due to nonmagnetic species (vacancies, Zn^{2+}). MAE, extrapolated from the usual value of γ - Fe_2O_3 in bulk and at room temperature taking account both nonmagnetic substitution and dependence on temperature, was shown to be the main contribution to the energy barrier of superparamagnetic relaxation. The inverse of the attempt frequency, exhibiting a lower value than those usually reported, has been explained by the extended Brown model^[36] assuming a realistic value for the damping constant.

2.2. LP Particles

As explained in the introduction, EG was added in the mix before microwave heating to obtain larger nanoparticles. To better assess the effect of cationic disorder, we decided to observe it on two values of Zn substitution: the previous one taken for SP ($Zn_{0.4}Fe_{2.6}O_4$) and $Zn_{0.2}Fe_{2.8}O_4$. The respective LP nanoparticles are referred to as 0.4LP and 0.2LP in the following. As for the SP sample, the Zn/Fe ratio from ICP-AES and EDS-STEM was checked to be close to the theoretical one within experimental error. XRD was performed and interpreted through a Rietveld analysis to determine a size of 17 ± 1 nm. In TEM pictures (Figure 5), the irregular shape of LP nanoparticles showing density contrast suggests they are constituted of aggregated smaller units [like the nanograins (NG) of^[13]] in accordance with other syntheses using polyol addition. A mean diameter of 22 nm with a standard deviation of 11 nm was determined using Sturge’s criterion to partition the TEM observed sizes, more approximately than for SP particles because of the irregular shape. A volume-weighted mean diameter instead of a number-weighted one can also be computed; it is about 30 nm. This is approximately twice the Rietveld diameter: the LP nanoparticles are polycrystalline. Moreover, extended crystalline order over the aggregated smaller units is observed in the nanoparticles as seen in Figure 5c). The high-resolution TEM (HRTEM) images (Figure 5d,e) corresponding to adjacent nanograins show that the different nanocrystalline grains share common crystallographic directions evidencing an oriented attachment between NG-type crystals of

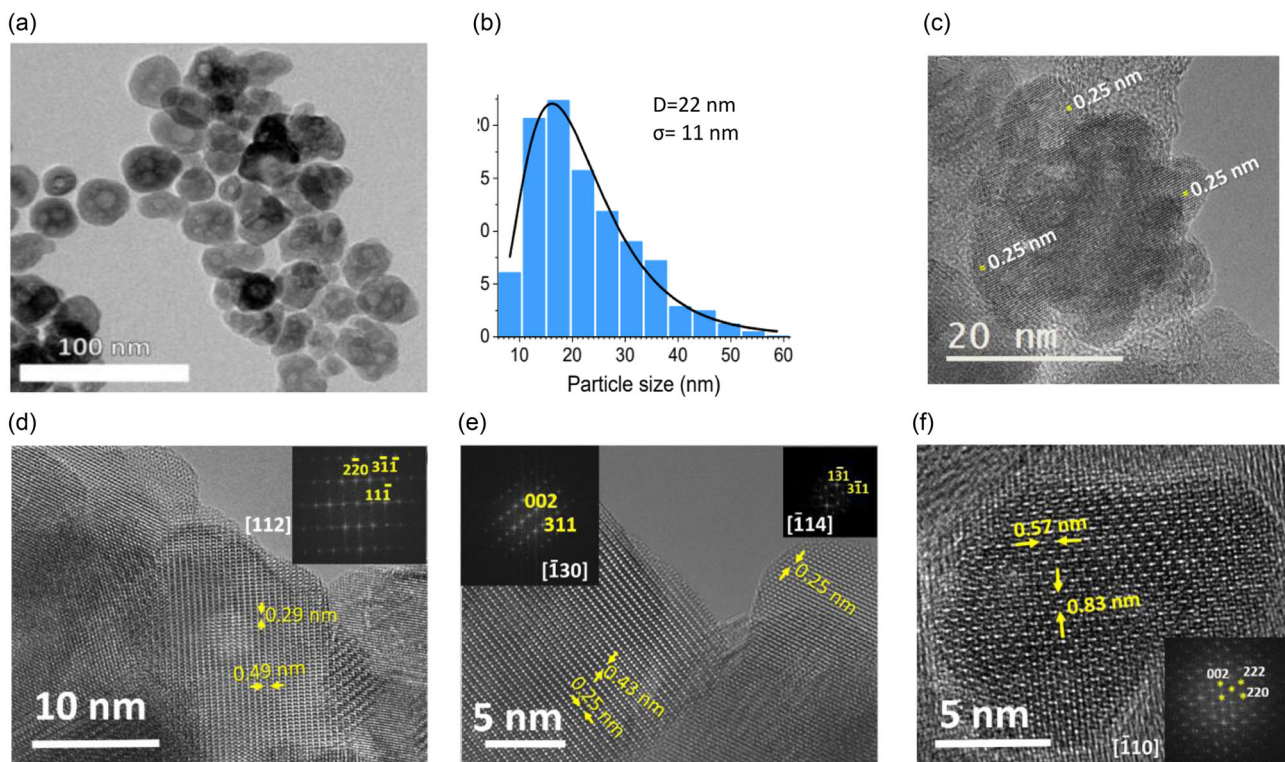


Figure 5. a) TEM observation of 0.4LP nanoparticles, b) size distribution retrieved from images on ≈ 1000 nanoparticles allowing to determine a mean size of 22 nm and a standard deviation of 11 nm, c) TEM image at higher magnification showing the coherent smaller units aggregation with crystalline order in the LP nanoparticle, d–f) HRTEM images of several connected particles showing the presence of common directions [311] and [002].

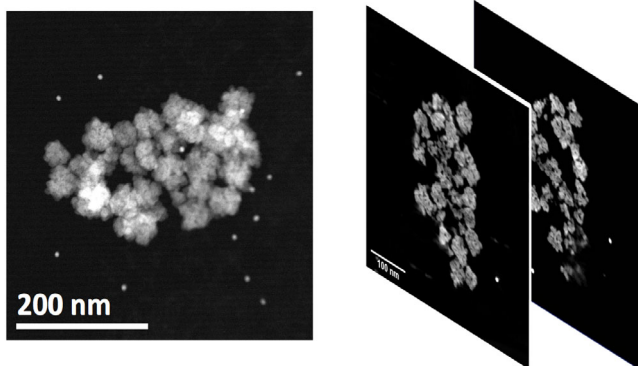


Figure 6. 3D analysis of an aggregate of nanoparticles by electron tomography. Left: typical STEM-HAADF image of the aggregate extracted from the tilt series of image projections used to reconstruct the volume. Right: two representative slices through the reconstructed volume, at different depths, illustrating the presence of a nanometric porosity within the particles and the nanoparticles assembling.

5 nm size, close to SP nanoparticles produced by the MATD reaction. This feature explains why the Rietveld diameter is close to the mean TEM diameter and not close to a smaller unit size of about ≈ 5 nm.

The inner structure of LP nanoparticles was observed by TEM tomography, as shown in **Figure 6**. Here, the inner structure appears to differ from the “raspberry” or “spherulite” one since the inner porosity repartition does not allow distinguishing clearly aggregated smaller units. As a comparison, in the 250 nm “raspberry,”^[13] the nanograins of 5 nm can be clearly observed, and the XRD analysis assesses their size. Here, it could be inferred from the shape of porosities that some of them seem to arise from 1) polyhedrals porosities arise from voids between packing of these smaller nanocrystals and 2) spherical porosities may be an inner porosity following an atomic diffusion from the inside of the NG to interfaces in order to minimize the interfacial

energy. In this concern, MATD synthesis with EG leads to nanoparticles LP with distributed size of small porosities and not to the hollow “raspberry” from the thermal decomposition route. A 3D reconstruction of the TEM slices was performed to determine both the volume fraction of porosity ($15 \pm 5\%$) and the distance between LP nanoparticles (50 ± 20 nm).

The STEM-HAADF study whose main results are presented in **Figure 7** focuses on the local atomic order. In **Figure 7a**, the continuity of atomic order at the interface between nanograins is exhibited. The atomically resolved image of a single particle is depicted in **Figure 7b** where the octahedral and tetrahedral positions are clearly observed, according to the spinel structure. The simultaneous EELS study suggests that Fe and Zn ions randomly occupy both octahedral and tetrahedral sites.

Mössbauer spectrometry was performed on both 0.4LP and 0.2LP to determine the oxidation level and the cationic repartition. The Mössbauer spectra recorded at 77 and 300 K are shown in **Figure 8a,b**, respectively. The hyperfine structure consists essentially in magnetic sextets with asymmetrical and broadened lines for the largest particles. At 77 K, the hyperfine structure exhibits a more resolved magnetic sextet attributed mostly to the presence of Fe^{3+} species with a magnetic blocked order. In addition, the shoulder of some lines (located at around -3 mm s^{-1}) is consistent with the presence of the Fe^{2+} component, as observed in the case of magnetite. The mean values of isomer shift allow to estimate the $\text{Fe}^{2+}/\text{Fe}^{3+}$ content^[38] in these assemblies of superparamagnetic Fe-containing nanoparticles: the $\text{Fe}^{2+}/\text{Fe}^{3+}$ ratio values estimated at 300, 77 and 14 K are quite similar but the most accurate value corresponds to that obtained at 14 K in the presence of external magnetic field (**Figure 8c**) since the different magnetic components are completely resolved unlike at 300 and 77 K, and the Lamb-Mössbauer factor values of these different components are the same.

Fitting parameters of in-field Mössbauer spectra in addition to the Fe^{2+} and Fe^{3+} ratio determined in this way are summed up in **Table 1** for all samples (see **Section 4**).

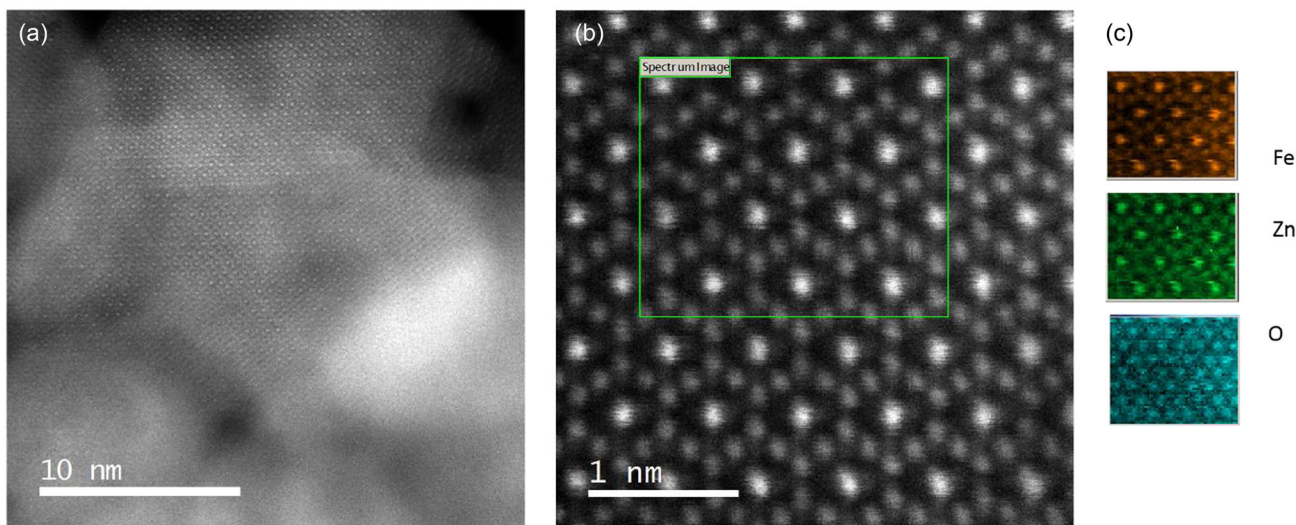


Figure 7. STEM HAADF-EELS study a) HAADF image at medium magnification; b) atomically resolved HAADF image; and c) EELS chemical maps of a nanoparticle oriented along [101].

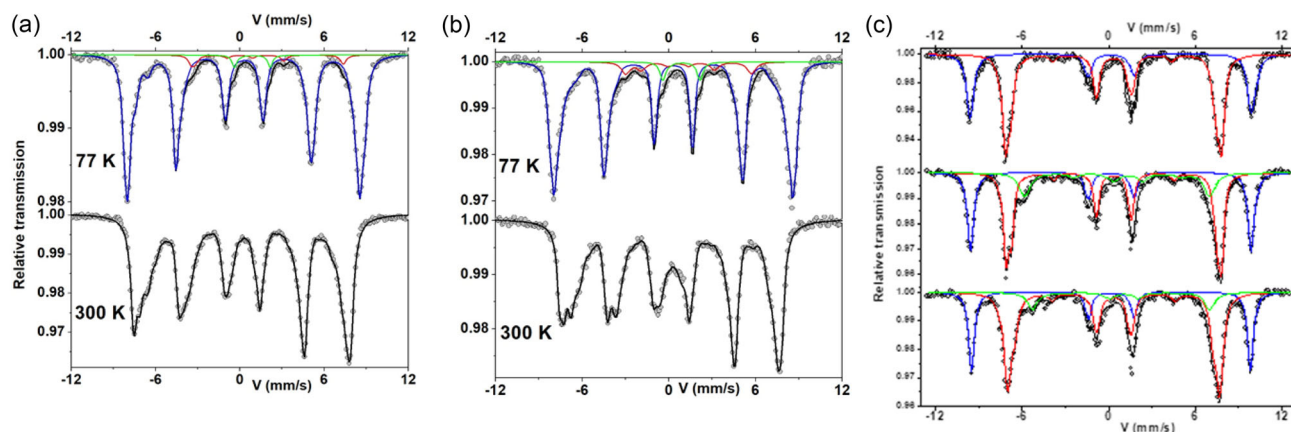


Figure 8. Mössbauer spectra a) at 77 and 300 K for 0.2LP, b) at 77 and 300 K for 0.4LP, and c) at 14 K under an 8 T external magnetic field applied parallel to the γ -beam for (from top to bottom) SP, 0.2LP and 0.4LP. In a,b) the blue, red, and green lines represent for Fe^{3+} and blocked Fe^{2+} contributions and a Fe^{2+} impurity, respectively; in c), the blue, red, and green lines represent the Fe^{3+} ions located at the tetrahedral and octahedral sites and the Fe^{2+} contribution, respectively.

Table 3. Size, cationic distribution, and magnetic moment for LP nanoparticles.

Size [nm]	Cationic distribution	Magnetic moment (at 2 K) $\mu_B/f.u$
From TEM 22 ± 11	0.4LP theoretical ($\text{Zn}_{0.4}^{2+}\text{Fe}_{0.6}^{3+}[\text{Fe}_{0.6}^{2+}\text{Fe}_{1.4}^{3+}]\text{O}_4$)	Measured 3.83
	0.2LP theoretical ($\text{Zn}_{0.2}^{2+}\text{Fe}_{0.8}^{3+}[\text{Fe}_{0.8}^{2+}\text{Fe}_{1.2}^{3+}]\text{O}_4$)	Measured 3.55
From Rietveld 17 ± 1	f0.4LP From Mössbauer ($\text{Fe}_{0.74}^{3+}[\text{Fe}_{0.29}^{2+}\text{Fe}_{1.48}^{3+}]\text{Zn}_{0.4}^{2+}\square_{0.11}\text{O}_4$)	Computed 4.56
	0.2 LP from Mössbauer ($\text{Fe}_{0.84}^{3+}[\text{Fe}_{0.63}^{2+}\text{Fe}_{1.27}^{3+}]\text{Zn}_{0.2}\square_{0.06}\text{O}_4$)	Computed 4.23
	Completed with Rietveld	
	0.4LP: ($\text{Fe}_{0.74}^{3+}\text{Zn}_{0.21}^{2+}\square_{0.05}[\text{Fe}_{0.34}^{2+}\text{Fe}_{1.44}^{3+}\text{Zn}_{0.16}^{2+}\square_{0.06}]\text{O}_4$)	
0.2LP: ($\text{Fe}_{0.88}^{3+}\text{Zn}_{0.11}^{2+}\square_{0.01}[\text{Fe}_{0.65}^{2+}\text{Fe}_{1.22}^{3+}\text{Zn}_{0.08}^{2+}\square_{0.05}]\text{O}_4$)		

As for the SP sample, a Rietveld refinement taking into account the iron cationic repartition from Mössbauer spectrometry was then performed to achieve the full cationic repartition of the spinel 0.2LP and 0.4LP, these results are summarized in **Table 3**. The cationic disorder evidenced from EELS was then quantified. The amount of nonmagnetic species (Zn^{2+} or vacancies) on the B site remains low (0.24 for 0.4LP) in comparison with the magnetic one (1.75). This is consistent with the absence of A site canting deduced from Mössbauer spectra. Moreover, one can notice that the higher canting angle is found for Fe^{2+} in 0.2LP. Canting angle differences between the two compositions 0.2LP and 0.4LP may be understood in the frame of the Yafet–Kittel model considering the mean magnetic moment of both sublattices S_A and S_B for each composition. The fact that the Fe^{2+} magnetic moment is smaller than that of Fe^{3+} implies then that the $S_A S_B$ term in the expression of the exchange energy $J_{AB} S_A S_B$ is smaller in the 0.2LP case (and the mean J_{AB} for 0.2LP composition should be lower following the exchange energy coefficients determined for each cation^[39]), leading to a higher canting angle.

Table 3 summarizes the LP nanoparticles features. As for the SP case, the magnetic moment $M_{0.4LP\text{theo}}$ was predicted with the Yafet–Kittel model applied to the number of cations per formula unit in the spinel equivalent formula in each site, with their

mean canting angle. The relative gap between calculated and experiment magnetic moment is 19% for both samples. The magnetic moment increases with the level of Zn substitution, following the trend observed for bulk Zn-substituted ferrites, despite the repartition of nonmagnetic species on both sites.

To get an insight on the magnetic state of the whole LP nanoparticle, FC/ZFC curves (**Figure 9a**) and AC susceptibilities were acquired (**Figure 9b**), and the latter were fitted by the Néel–Brown model (**Figure 9c**).

From the ZFC/FC curves, a clear blocking behavior is not evidenced, as already observed for nanoparticles of similar size.^[31] The fact the blocking temperature cannot be easily identified is related to the dispersion of reversal times, which could be due to the peculiar morphology of the LP nanoparticles, or to the dispersion of LP nanoparticles size (intrinsic relaxation) and distances (dipolar coupling). However, as in^[31] for spherical nanoparticles the same behavior is observed, we can exclude an effect of the morphology. If the distance between SP nanoparticles seems to be quite constant due to the agglomeration of nanoparticles limited by the surfactant coating, the LP nanoparticles do not aggregate, and then we can attribute mainly the broadening to the size and diameter dispersion. Lastly, the broadening effect is certainly enhanced by the variation of the magnetization and MAE with temperature.

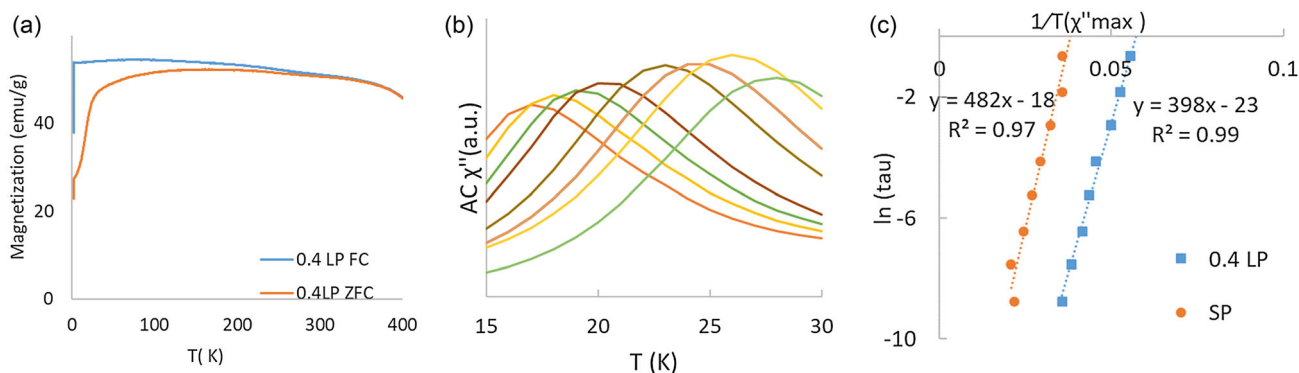


Figure 9. SQUID VSM characterization of 0.4LP nanoparticles: a) FC/ZFC curves, b) AC imaginary susceptibility, and c) fits performed for both SP and 0.4LP on the deduced relation of $\frac{1}{T_{\chi''_{\max}}}$ versus $\ln(\tau)$.

AC susceptibilities exhibit an imaginary susceptibility peak occurring at ≈ 30 K depending on the frequency. The inverse temperature of the maximum of AC imaginary susceptibility peak is linearly correlated, with a great accuracy, to the logarithm of the inverse measurement frequency of the susceptibility. Interpreting it with $\tau = \tau_0 \exp\left(\frac{E_B}{k_B T}\right)$, the energy barrier E_B/k_B of ≈ 386 K and τ_0 of 1.25×10^{-10} s are obtained.

Since the porosity volume fraction is quite low (15%), and since the observed high degree of atomic order could lead to a strong exchange coupling, LP could behave like dense nanoparticles. The first possible interpretation for the AC susceptibility is to explain the energy barrier with the effective anisotropy and the mean volume: $E_b = K_{\text{eff}} V$, as we did in the SP case. Using the TEM diameter of 22 nm for the volume and corrected with the 15% porosity, an effective anisotropy of $\approx 1 \text{ kJ m}^{-3}$ is found. Using the Rietveld crystallite size of 17 nm to account for the porosity but assuming a single crystalline domain in the nanoparticle, the effective anisotropy energy would be of 2.1 kJ m^{-3} . In both cases, the values are unusually low (remembering that it was of $\approx 100 \text{ kJ m}^{-3}$ for SP nanoparticles, $\approx 3 \text{ kJ m}^{-3}$ for magnetite at room temperature, that is, $15\text{--}20 \text{ kJ m}^{-3}$ is expected for a substituted magnetite at 90 K). Moreover, for similar nanoparticles labeled “F2”,^[40] synthesized by classical thermal decomposition with the same theoretical composition than 0.4LP and close in diameter (26 nm), it was found from AC susceptibility that $T_B = 188$ K and $K_{\text{eff}} = 18.8 \text{ kJ m}^{-3}$, consistent with bulk MAE.^[34] To our opinion, the observed relaxation of 0.4LP at ≈ 20 K seems not be accounted for by a classical superparamagnetic relaxation.

As the room temperature VSM loop has a classical shape for blocked nanoparticles, and the ZFC magnetization curve exhibits a nonzero value at 2 K, another hypothesis is that coupling between nanoparticles could lead to a partial magnetic order in the sample that could be relaxed too.

We therefore consider the dipolar energy in 0.4LP sample with $E_d = \frac{\mu_0}{4\pi} n_1 \frac{\mu^2}{d^3}$ as for SP nanoparticles. The value of M_s deduced from the specific magnetization, the actual molar mass (taking oxidization into account), and the lattice parameter deduced from the Rietveld fit, that is, 8.408 nm for 0.4LP (0.8398 nm for 0.2 LP), is 478 kA m^{-1} (444 kA m^{-1} for 0.2LP).

The usual TEM images show a superposition of the nanoparticles, which prevents the determination of an average interparticle distance and of the number of neighbors. However, from the electron tomography pictures (Figure 6), one can observe clearly that the LP particles are not close-packed, with an approximate number of first neighbors of 6 close to the one of a nondense simple cubic packing of spheres. Using the center-to-center interparticle distance of 50 ± 20 nm determined from TEM tomography image analysis, the computation of dipolar energy, taking the volume corrected from porosity gives for the magnetic moment gives ≈ 2000 K. Taking the Rietveld diameter, which seems to us more accurate since some amorphous or nonmagnetic phase may contribute to the TEM diameter, to compute the volume leads to 500 K, which is close to the experimental value of 386 K. Moreover, the third power on the interparticle distance in the expression of the dipolar energy leads to a great lack of precision: in this last case, its value spreads from 190 K for a 70 nm interparticle distance to 2500 K for 30 nm.

In other cases, porosity can change drastically the magnetic behavior: the magnetic state of “raspberry” nanoparticles exhibits features of a super-spin glass state arising from the strong dipolar coupling between the NG.^[41] Quasi-perfect hollow iron oxide nanoparticles show a spin glass-like behavior, with higher blocking energy of spin clusters at the inner and outer surfaces.^[42] In both cases, the AC susceptibility dependence with frequency is better described by a Fulcher–Vogel law than with a linear relation of $\ln(\tau)$ versus $1/T_{\chi''_{\max}}$. In our case, considering the excellent agreement of the linear relation with a 0.99 correlation ratio, more complex models suggesting spin-glass-like relaxation are not likely needed. The observed relaxation seems then to be due to the dipolar coupling between LP nanoparticles.

The measured relaxation time τ_0 of $\approx 1.25 \times 10^{-10}$ s was not interpreted using Coffey’s model, since we showed for SP that coupling effects could be involved, as in LP they are much larger.

Lastly, applying $K_{\text{eff}} = \frac{\ln(\frac{\tau_0}{\tau}) k_B}{V T_B}$ with this attempt frequency and the temperature T_B at which FC and ZFC curves merge (≈ 250 K), we obtain $\approx 30 \text{ kJ m}^{-3}$ which could be then interpreted as the actual LP superparamagnetic relaxation with a MAE barrier. This value is in the same range than for nonoxidized

nanoparticles^[40] but a bit higher than the $\approx 11 \text{ kJ m}^{-3}$ observed for a bulk Zn_{0.4}-substituted magnetite.^[34]

In this part, it was shown by electron tomography that LP nanoparticles synthesized by EG addition during the MATD exhibit a peculiar morphology looking as an aggregation of smaller units, similarly to other nanoparticles (raspberry, spherulite) synthesized by close chemical routes. LP nanoparticles differ from those cases in particular by an epitaxy relation over 20% of the nanoparticle volume (ratio of the Rietveld diameter based volume to the TEM mean volume). This may be the result of an oriented attachment mechanism, if the HRTEM images of Figure 5c–f) are representative of the whole set of LP nanoparticles. Thanks to image analysis of electron tomography pictures, a porosity fraction of 15% and a mean interparticle distance of 50 nm were determined. Partial oxidation with a loss of Fe²⁺ of $\approx 50\%$ was deduced from Mössbauer fits. Cationic disorder of Zn²⁺ was deduced from analysis of EELS-HAADF implemented on STEM, and Rietveld analysis was applied to determine the full cationic order including vacancies. The measured magnetic moment at 2 K was successfully compared with the one computed from a Yafet–Kittel model taking the Mössbauer canting angle as a mean volume canting. The magnetic behavior of the whole nanoparticle was characterized by AC susceptibility. The observed relaxation at 25 K has been discussed and has been attributed to dipolar coupling between LP nanoparticles. The value of the effective anisotropy was computed from the measured relaxation time with an excellent agreement with the measured energy barrier. The LP nanoparticles remain blocked at 300 K for a fast measurement time of 10^{-8} s like in microwave permeability measurements.^[43]

3. Conclusion

In this work, we have attempted to relate the magnetic properties to the atomic and nanoscale structural characteristics of two nanoparticle systems. Instead of using approximations and commonly assumed sources of discrepancies (surface anisotropy, dispersion, cationic disorder, dipolar coupling, etc.), we succeeded in understanding the magnetic characteristics using simple models for the energy barrier based on various and dedicated characterizations. Moreover, for SP nanoparticles, we compared the effective anisotropy determined from the relaxation time either by the Néel–Brown model or by an extended Brown model derived by Coffey. It seems that dynamic dipolar coupling could strongly affect the prediction of Coffey model, even if the static dipolar energy remains small in comparison to the magnetocrystalline energy. Lastly, despite their apparent structural complexity, the behavior of LP nanoparticles was successfully interpreted by applying classical models valid for dense nanoparticles.

4. Experimental Section

SP and LP Nanoparticles Synthesis: Iron acetylacetonate ([Fe(acac)₃], 97% purity), zinc acetylacetonate hydrate [Zn(acac)₂], oleic acid (OA, 90% purity), and ethyl acetate and ethylene glycol were purchased from Sigma Aldrich, absolute ethanol from VWR, 1-octadecene (ODE) from Merck Millipore, and oleylamine (OAm, 90% purity) from Acros Organics. The synthesis method of Zn_xFe_{3-x}O₄ nanoparticles was derived from^[16]

Table 4. Ratio of [Zn(acac)₂] and EG used for the synthesis of SP, 0.4LP, and 0.2 LP.

Name	[Zn(acac) ₂]/[Fe(acac) ₃]	EG/[Fe(acac) ₃]
SP	0.15	0
0.4LP	0.15	36
0.2LP	0.07	36

which deals with the synthesis of Fe₃O₄ nanoparticles through MATD. In this method, oleylamine (OAm), OA, and ODE with the molar ratio of ODE/[Fe(acac)₃] = 19, Oam/[Fe(acac)₃] = 24, OA/[Fe(acac)₃] = 6 were homogeneously mixed and various quantities of and EG were added as given in Table 4.

For a reactor volume of 20 mL, the following quantities were used: 1 mmol [Fe(acac)₃], 0.15 mmol [Zn(acac)₂], 8 mL OAm, 2 mL OA, and 6 mL ODE.

After a 10 min ultrasonic homogenization, the solution was introduced into the microwave reactor Monowave 300 (Anton-Paar). The mixture was at first heated up to 200 °C at 40 °C min⁻¹ and then held at this temperature for 10 min. Then, the temperature was increased to 270 °C at 14 °C min⁻¹ and held for 15 min. The reactor was finally cooled down to 60 °C. After synthesis, the nanoparticles were recovered and washed six times by centrifugation steps with addition of a mixture of 73%v of ethyl acetate and 27%v of ethanol. The number of washing steps was determined by following the decrease of the organics IR signal. Then, the nanoparticles were dried naturally under air. The thermo-gravimetric analyses (TGA) of the SP and LP nanoparticles under helium were compared with the one of pure OA. A weight loss was observed, 24% for SP and 6% for 0.4LP, corresponding to the degradation temperature of OA. This measured weight loss can be converted into an equivalent number of oleate layers at the nanoparticle surface: we assumed^[44] that the adsorbed OA molecule carboxylic head has an equivalent area of 24 Å²; the oleate length is 2 nm, which gives a 480 Å³ volume. Then, using the mean TEM diameter of the nanoparticles, the equivalent number of oleate monolayers was 0.9 for SP and 0.7 for LP. Figure 1 and graphical abstract were drawn using Biorender.

XRD and Rietveld Analysis: The XRD measurements were carried out on a D8 Discover diffractometer in Bragg Brentano geometry equipped with a Cu sealed tube ($\lambda_{\text{CuK}\alpha 1} = 1.54059 \text{ \AA}$), a quartz front monochromator, a motorized anti-scatter screen and an energy resolved Lynxeye XE-T linear detector in the 18°–90°(2 θ) range with a scan step of 0.02°. Rietveld refinements were performed through the Fullprof program^[45] with the modified Thompson–Cox–Hasting (TCH) pseudo-Voigt profile function^[46] and are shown in Figure 10. The instrumental resolution function (IRF) was generated using an Al₂O₃ corundum standard and inserted in the PCR file.

In order to converge towards the most probable solution, the Rietveld strategy for the refinement was the following: 1) the distribution of the iron atoms was fixed to that obtained by Mossbauer spectrometry and 2) The Zn content was calculated by $[\text{Zn}] = xR$. This quantity was distributed between the two sites $[\text{Zn}]_A + [\text{Zn}]_B = xR$. This was the only free parameter for cation refinements; and 3) the distribution of Zn in the two sites allowed us to calculate the vacancies as $[\text{Fe}]_A + [\text{Zn}]_A + [\text{vacancies}]_A = 1$ (i.e., full occupancy) and $[\text{Fe}]_B + [\text{Zn}]_B + [\text{vacancies}]_B = 1$.

The standard deviations are given in parentheses for each sample:

$$\text{LP02: } [\text{Zn}]_A = 0.116(6); [\text{Zn}]_B = 0.080(6); a = 0.8398(1) \text{ nm} \quad (4)$$

$$\text{LP04: } [\text{Zn}]_A = 0.207(5); [\text{Zn}]_B = 0.179(5); a = 0.8408(1) \text{ nm} \quad (5)$$

$$\text{SP: } [\text{Zn}]_A = 0.137(15); [\text{Zn}]_B = 0.235(14); a = 0.8396(2) \text{ nm} \quad (6)$$

Magnetic Measurements: VSM and AC magnetization measurements were carried out using a Quantum Design superconducting quantum interference device magnetometer (MPMS SQUID VSM), equipped with a superconducting magnet ($H_{\text{max}} \pm 7 \text{ T}$). Powder samples were

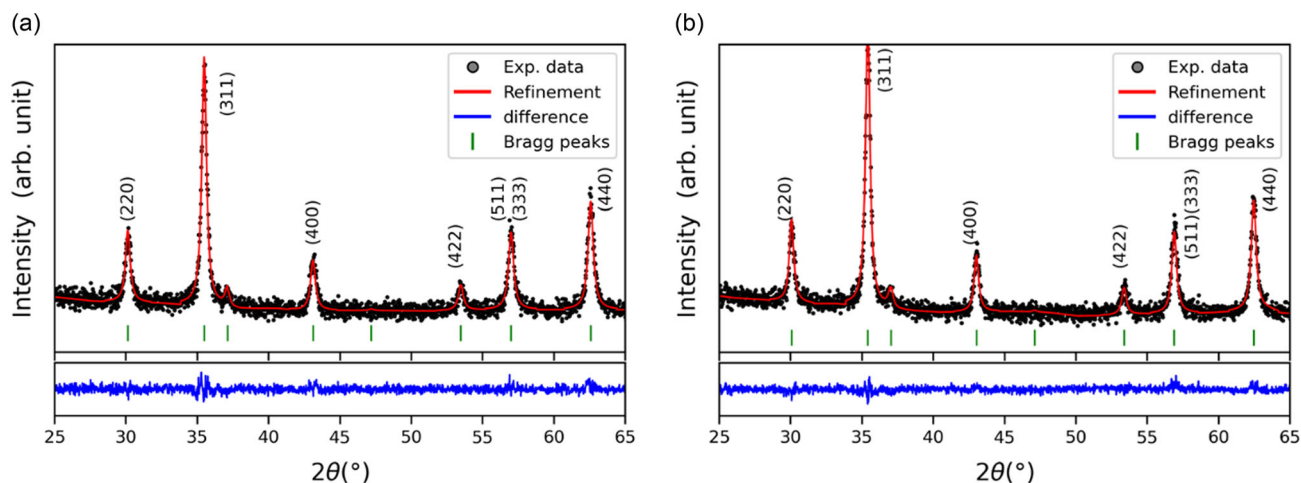


Figure 10. RX diffractograms with Rietveld refinement for a) 0.2LP and b) 0.4LP.

encapsulated in standard capsules which were then inserted in manufacturer-provided plastic straws. For the magnetization versus temperature measurements, ZFC and FC protocols were used in the VSM mode. To perform ZFC measurements, the sample was first cooled from room temperature down to 5 K in zero-field, then the magnetization (M_{ZFC}) was recorded in VSM mode warming up from 5 to 300 K, with a static 500 G applied magnetic field. For the FC measurements, the sample was cooled from room temperature to 5 K under an external 500 G magnetic field and the magnetization M_{FC} was recorded during the subsequent heating from 5 to 300 K. In AC measurements, the modulation field was set to 2 G and 10 frequencies values were scanned from 0.1 Hz to 1 kHz at each temperature, from 15 to 50 K and under no external static field.

Magnetic hysteresis curves ($H_{max} \pm 7$ T) were measured in VSM mode at 2 and 300 K to determine the saturation magnetization, with a 2 s measurement time.

Mössbauer Spectrometry: ^{57}Fe transmission Mössbauer spectrometry was carried out using a conventional device with a $^{57}\text{Co}/\text{Rh}$ source mounted on a transducer that oscillates with constant acceleration. The samples consist of a thin and homogeneous layer of powdered nanoparticles containing about 5 mg Fe/cm^2 . Mössbauer spectra were obtained at 300, at 77 K using a bath cryostat and then at 14 K under an 8 T magnetic field using a cryomagnetic device where the external field is oriented parallel to the γ -beam. The velocity of the spectrometer was calibrated by using a thin foil of α -Fe. The experimental spectra were analyzed by a least square fitting method (using the unpublished MOSFIT program) based on quadrupolar and magnetic components with Lorentzian lines (the values of isomer shift are referred to that of α -Fe at 300 K).

Transmission Electron Microscopy: The nanoparticle morphology and size were observed by transmission electron microscopy (TEM) using a JEOL JEM-2100F TEM with a Gatan UltraScan 4k camera. The nanoparticle size was first evaluated with the ImageJ software. 150–750 particles are recorded per sample and the sizes are averaged over 5–7 samples originating from different synthesis batches. The final distribution is calculated from 1000 to 2500 particles. Following,^[47] the Sturge partition criterion is used to define k size classes of width W , with $k = 1 + 3.322 \times \log(N)$ and $W = \frac{D_{max} - D_{min}}{k}$, and N the number of assessed particles. The total number of classes k was found to be 13 for SP and 12 for 0.4LP particles. Fitting this distribution with a log-normal distribution allows obtaining its mean diameter and standard deviation.

The STEM of the National Center for Electron Microscopy (ICTS) at the Complutense University of Madrid (UCM) was used in combination with the high-angle annular dark-field imaging (HAADF) technique. Coupled to

electron energy loss spectroscopy (EELS), it allows to deduce the position of atoms in the crystalline structure, here applied to determine the position of iron and zinc cations in the 0.4LP. As the Zn-L_{2,3} edge is too weak and hard to distinguish in the EELS spectra, the detection of Zn was achieved through some adjustments of the device as the use of two energy windows and at the same time by changing the spot size. Zn is hence detected even if its signal remains noisy. The relative intensity of the peaks corresponding to Fe-L_{2,3} edge matches with the one obtained for Fe_3O_4 in the literature^[48] ($\text{Fe}^{3+}/\text{Fe}^{2+}$), which depicts the measurement reliability and quality.

The electron tomography analysis was carried out using a JEOL 2100 FEG S/TEM microscope operated at 200 kV, equipped with a probe aberration corrector. The samples were dispersed by ultrasonication in ethanol and deposited on holey carbon-coated TEM grids. The STEM images were obtained using a spot size of 0.1 nm, a current density of 54 pA and a camera focal length of 12 cm, corresponding to inner and outer diameters of the annular detector of about 52 and 140 mrad. The acquisition of tilt series was performed by using the tomography plug-in of the Digital Micrograph software, which controls the specimen tilt step by step, the defocusing and the specimen drift. The HAADF images in the STEM mode were acquired by tilting the specimen within a 120° angular range using an increment of 2° in the equal mode, giving thus a total number of 60 images in each series. The as-recorded projection images were spatially aligned by using cross correlation algorithms in the IMOD software. For the volume calculation, the Tomoj plugin implemented in the ImageJ software was used. Finally, the visualization and the analysis of the final reconstructions were carried out using the displaying capabilities and the isosurface rendering method available in the Slicer software.

Conflict of Interest

The authors declare no conflict of interest.

Data Availability Statement

The data that support the findings of this study are available from the corresponding author upon reasonable request.

Keywords

AC magnetic susceptibility, electron tomography, iron oxide nanoparticles, thermal decomposition synthesis

Received: March 1, 2024
Revised: June 14, 2024
Published online:

- [1] Q. A. Pankhurst, J. Connolly, S. K. Jones, J. Dobson, *J. Phys. D: Appl. Phys.* **2003**, 36, R167.
- [2] M. K. Yu, D. Kim, I.-H. Lee, J.-S. So, Y. Y. Jeong, S. Jon, *Small* **2011**, 7, 2241.
- [3] X. Wei, M.-L. Jin, H. Yang, X.-X. Wang, Y.-Z. Long, Z. Chen, *J. Adv. Ceram.* **2022**, 11, 665.
- [4] B. Barbara, *Solid State Sci.* **2005**, 7, 668.
- [5] L. Gonzalez-Moragas, S.-M. Yu, N. Murillo-Cremaes, A. Laromaine, A. Roig, *Chem. Eng. J.* **2015**, 281, 87.
- [6] R. Pauthenet, *Ann. Phys.* **1952**, 12, 710.
- [7] E. W. Gorter, *Philips Res. Rep.* **1954**, 9, 295.
- [8] R. Sai, S. D. Kulkarni, M. Yamaguchi, N. Bhat, S. A. Shivashankar, *IEEE Magn. Lett.* **2017**, 8, 1.
- [9] V. G. Harris, V. Šepelák, *J. Magn. Magn. Mater.* **2018**, 465, 603.
- [10] G. Cotin, F. Perton, C. Petit, S. Sall, C. Kiefer, V. Begin, B. Pichon, C. Lefevre, D. Mertz, J.-M. Greneche, S. Begin-Colin, *Chem. Mater.* **2020**, 32, 9245.
- [11] A. Demortière, P. Panissod, B. P. Pichon, G. Pourroy, D. Guillon, B. Donnio, S. Bégin-Colin, *Nanoscale* **2011**, 3, 225.
- [12] M. E. F. Brollo, S. Veintemillas-Verdaguer, C. M. Salván, *Contrast Media Mol. Imaging* **2017**, 2017, 8902424.
- [13] O. Gerber, B. P. Pichon, D. Ihiawakrim, I. Florea, S. Moldovan, O. Ersen, D. Begin, J.-M. Grenèche, S. Lemonnier, E. Barraud, S. Begin-Colin, *Nanoscale* **2017**, 9, 305.
- [14] A. Yan, X. Liu, R. Yi, R. Shi, N. Zhang, G. Qiu, *J. Phys. Chem. C* **2008**, 112, 8558.
- [15] S.-H. Yu, Q.-L. Wang, Y. Chen, Y. Wang, J.-H. Wang, *Mater. Lett.* **2020**, 278, 128431.
- [16] Y.-J. Liang, F. Fan, M. Ma, J. Sun, J. Chen, Y. Zhang, N. Gu, *Colloids Surf., A* **2017**, 530, 191.
- [17] O. Ersen, I. Florea, C. Hirlimann, C. Pham-Huu, *Mater. Today* **2015**, 18, 395.
- [18] Y. Yang, X. Liu, Y. Yang, W. Xiao, Z. Li, D. Xue, F. Li, J. Ding, *J. Mater. Chem. C* **2013**, 1, 2875.
- [19] P. A. Borisova, S. S. Agafonov, M. S. Blanter, V. A. Somenkov, *Phys. Solid State* **2014**, 56, 199.
- [20] P. Poix, *Bull. Soc. Chim. Fr.* **1965**, 2, 1085.
- [21] C. J. Goss, *Phys. Chem. Miner.* **1988**, 16, 164.
- [22] W. O'Reilly, *Phys. Earth Planet. Inter.* **1983**, 31, 65.
- [23] E. Tronc, P. Prené, J. P. Jolivet, J. L. Dormann, J. M. Grenèche, *Hyperfine Interact.* **1998**, 112, 97.
- [24] J. Salafranca, J. Gazquez, N. Pérez, A. Labarta, S. T. Pantelides, S. J. Pennycook, X. Batlle, M. Varela, *Nano Lett.* **2012**, 12, 2499.
- [25] G. Alvarez, H. Montiel, J. F. Barron, M. P. Gutierrez, R. Zamorano, *J. Magn. Magn. Mater.* **2010**, 322, 348.
- [26] Y. Yafet, C. Kittel, *Phys. Rev.* **1952**, 87, 290.
- [27] M. P. Morales, S. Veintemillas-Verdaguer, M. I. Montero, C. J. Serna, A. Roig, L. Casas, B. Martínez, F. Sandiumenge, *Chem. Mater.* **1999**, 11, 3058.
- [28] C. E. Patton, Y. Liu, *J. Phys. C: Solid State Phys.* **1983**, 16, 5995.
- [29] J. L. Dormann, D. Fiorani, E. Tronc, *Adv. Chem. Phys.* **1997**, 98, 293.
- [30] I. J. Bruvera, P. Mendoza Zélis, M. Pilar Calatayud, G. F. Goya, F. H. Sánchez, *J. Appl. Phys.* **2015**, 118, 184304.
- [31] G. F. Goya, T. S. Berquó, F. C. Fonseca, M. P. Morales, *J. Appl. Phys.* **2003**, 94, 3520.
- [32] J. L. Dormann, L. Bessais, D. Fiorani, *J. Phys. C: Solid State Phys.* **1988**, 21, 2015.
- [33] S. Krupicka, K. Zaveta, in *Magnetic Oxides*, Wiley, New York **1975**.
- [34] N. Miyata, *J. Phys. Soc. Japan* **1961**, 16, 1291.
- [35] S. Bedanta, W. Kleemann, *J. Phys. D: Appl. Phys.* **2009**, 42, 013001.
- [36] W. T. Coffey, D. S. F. Crothers, Yu. P. Kalmykov, E. S. Massawe, J. T. Waldron, *Phys. Rev. E* **1994**, 49, 1869.
- [37] M. Nagata, T. Ono, K. Tanabe, T. Moriyama, D. Chiba, J.-I. Ohe, M. Myoka, T. Niizeki, H. Yanagihara, E. Kita, *IEEE Trans. Magn.* **2014**, 50, 1.
- [38] J. Fock, L. K. Bogart, D. González-Alonso, J. I. Espeso, M. F. Hansen, M. Varón, C. Frandsen, Q. A. Pankhurst, *J. Phys. D: Appl. Phys.* **2017**, 50, 265005.
- [39] G. F. Dionne, *J. Appl. Phys.* **2006**, 99, 08M913.
- [40] I. Sharifi, A. Zamanian, A. Behnamghader, *J. Magn. Magn. Mater.* **2016**, 412, 107.
- [41] O. Gerber, B. P. Pichon, C. Ulhaq, J.-M. Grenèche, C. Lefevre, I. Florea, O. Ersen, D. Begin, S. Lemonnier, E. Barraud, S. Begin-Colin, *J. Phys. Chem. C* **2015**, 119, 24665.
- [42] H. Khurshid, P. Lampen-Kelley, Ö. Iglesias, J. Alonso, M.-H. Phan, C.-J. Sun, M.-L. Saboungi, H. Srikanth, *Sci. Rep.* **2015**, 5, 15054.
- [43] M. Darcheville, A.-L. Adenot-Engelvin, C. Boscher, N. Vukadinovic, C. Lefevre, A. Thiaville, C. Sanchez, *IEEE Magn. Lett.* **2020**, 11, 1.
- [44] L. Zhang, R. He, H.-C. Gu, *Appl. Surf. Sci.* **2006**, 253, 2611.
- [45] J. Rodríguez-Carvajal, *Phys. B* **1993**, 192, 55.
- [46] P. Thomson, D. E. Cox, J. B. Hastings, *J. Appl. Cryst.* **1987**, 20, 79.
- [47] F. H. Aragón, J. A. H. Coaquira, L. Villegas-Lelovsky, S. W. da Silva, D. F. Cesar, L. C. C. M. Nagamine, R. Cohen, E. Menéndez-Proupin, P. C. Morais, *J. Phys.: Condens. Matter* **2015**, 27, 095301.
- [48] C. Colliex, T. Manoubi, C. Ortiz, *Phys. Rev. B* **1991**, 44, 11402.